PHYSICAL REVIEW C **88**, 044331 (2013)

Low-lying dipole strength of the open-shell nucleus ^{94}Mo

C. Romig,[1,*] J. Beller,[1] J. Glorius,[2] J. Isaak,[3,4] J. H. Kelley,[5,6] E. Kwan,[6,7,†] N. Pietralla,[1] V. Yu. Ponomarev,[1] A. Sauerwein,[2]
D. Savran,[3,4] M. Scheck,[1,8,9] L. Schnorrenberger,[1] K. Sonnabend,[2] A. P. Tonchev,[6,7,‡] W. Tornow,[6,7] H. R. Weller,[6,7]
A. Zilges,[10] and M. Zweidinger[1]
[1]*Institut für Kernphysik, Technische Universität Darmstadt, D-64289 Darmstadt, Germany*
[2]*Institut für angewandte Physik, Goethe Universität Frankfurt am Main, D-60438 Frankfurt am Main, Germany*
[3]*ExtreMe Matter Institute EMMI and Research Division, GSI Helmholtzzentrum für Schwerionenforschung GmbH,*
D-64291 Darmstadt, Germany
[4]*Frankfurt Institute for Advanced Studies FIAS, D-60438 Frankfurt am Main, Germany*
[5]*Department of Physics, North Carolina State University, Raleigh, North Carolina 27695, USA*
[6]*Triangle Universities Nuclear Laboratory, Durham, North Carolina 27708, USA*
[7]*Department of Physics, Duke University, Durham, North Carolina 27708, USA*
[8]*School of Engineering, University of the West of Scotland, Paisley PA1 2BE, United Kingdom*
[9]*SUPA, Scottish Universities Physics Alliance, Glasgow G12 8QQ, United Kingdom*
[10]*Institut für Kernphysik, Universität zu Köln, D-50937 Köln, Germany*

(Received 15 August 2013; published 29 October 2013)

The low-lying dipole strength of the open-shell nucleus ^{94}Mo was studied via the nuclear resonance fluorescence technique up to 8.7 MeV excitation energy at the bremsstrahlung facility at the Superconducting Darmstadt Electron Linear Accelerator (S-DALINAC), and with Compton backscattered photons at the High Intensity γ-ray Source (HIγS) facility. In total, 83 excited states were identified. Exploiting polarized quasi-monoenergetic photons at HIγS, parity quantum numbers were assigned to 41 states excited by dipole transitions. The electric dipole-strength distribution was determined up to 8.7 MeV and compared to microscopic calculations within the quasiparticle phonon model. Calculations and experimental data are in good agreement for the fragmentation, as well as for the integrated strength. The average decay pattern of the excited states was investigated exploiting the HIγS measurements at five energy settings. Mean branching ratios to the ground state and first excited 2_1^+ state were extracted from the measurements with quasi-monoenergetic photons and compared to γ-cascade simulations within the statistical model. The experimentally deduced mean branching ratios exhibit a resonance-like maximum at 6.4 MeV which cannot be reproduced within the statistical model. This indicates a nonstatistical structure in the energy range between 5.5 and 7.5 MeV.

DOI: 10.1103/PhysRevC.88.044331 PACS number(s): 23.20.Lv, 24.60.−k, 25.20.Dc, 27.60.+j

I. INTRODUCTION

Low-lying dipole strength is a commonly observed feature of the structure of atomic nuclei. The electric part of the nuclear dipole response is dominated by the isovector electric giant dipole resonance (IVGDR) [1], exhausting nearly 100% of the Thomas-Reiche-Kuhn (TRK) sum rule [2] for isovector electric dipole transitions. However, a concentrated enhancement of electric dipole strength below the neutron separation threshold S_N was reported for many nuclei. Since this concentration of strength has a resonance-like shape, it is often referred to as pygmy dipole resonance (PDR).

First indications for the PDR were already observed about five decades ago. Bartholomew and co-workers found an enhancement of γ-ray strength in the γ decay after thermal neutron-capture reactions in various nuclei (see, e.g., [3]). A few years later this phenomenon was denoted as "pigmy resonance" [4,5]. Nowadays, the PDR is widely accepted as a new, common mode of excitation of atomic nuclei [6]. A frequently used geometrical picture of the PDR is an out-of-phase oscillation of excess neutrons against an isospin saturated core [7]. However, although it is already observed in many nuclei and reproduced in many microscopic model calculations (see, e.g., Ref. [8] and references therein), its nature is still under discussion.

Real photons, as probes of the nuclear structure, are highly sensitive to dipole excited states due to their low angular momentum transfer. Thus, the method of real photon scattering or nuclear resonance fluorescence (NRF) is an ideal tool for the investigation of low-lying dipole strength [9,10]. In the last two decades, systematic investigations of many nuclei have been performed using NRF. An enhancement of electric dipole strength below S_N was found in many stable nuclei located throughout the nuclear chart. It was reported for the stable Ca [11,12], Ni [13–15], Ge [16], Mo [17,18], Sn [19,20], and Pb isotopes [21,22], as well as for the $N = 50$ isotones ^{86}Kr [23], ^{88}Sr [24], ^{89}Y [25], and ^{90}Zr [26], and the $N = 82$ isotones [27–30].

With the advent of Coulomb excitation experiments in inverse kinematics using exotic beams, the investigation of low-lying dipole strength was extended to very neutron-rich

---

[*] romig@ikp.tu-darmstadt.de

[†] Present address: National Superconducting Cyclotron Laboratory, Michigan State University, East Lansing, Michigan 48824, USA.

[‡] Present address: Physics Division, Lawrence Livermore National Laboratory, Livermore, California 94550, USA.

(unstable) nuclei. In the isotopes $^{129-132}$Sn and ^{133,134}Sb [31,32], as well as in ^{68}Ni [33], the total strength in the energy range in which the PDR is located was reported to be higher than in less neutron-rich nuclei.

Very recently, $(\alpha,\alpha'\gamma)$ measurements were performed to study low-lying dipole strength, revealing a new feature of the PDR. In Refs. [34–36] a splitting of the PDR into two parts with different underlying structure is reported. This splitting is not fully understood yet, and the nature of the PDR remains a matter of ongoing discussion. For a more complete overview of the available experimental data we refer to Ref. [6].

Up to now, many experimenters, as well as theorists, have intensively studied low-lying dipole strength, especially in nuclei with at least one closed major shell. Otherwise, open-shell nuclei are rather rarely investigated with respect to the PDR [13,17,18,37]. In particular, data on individual excited states of such nuclei are sparse, since nuclei with no closed shells exhibit rather high level densities, enhancing the fragmentation of strength and, hence, making it considerably more difficult to resolve individual states in the experiment. Therefore, the PDR of open-shell nuclei is virtually unexplored up to date.

In this article, we report on our investigation of the low-lying dipole strength in the open-shell nucleus ^{94}Mo ($Z = 42$ protons and $N = 52$ neutrons) using NRF at the bremsstrahlung site of the S-DALINAC at TU Darmstadt, Germany, and using NRF with linearly polarized, quasi-monoenergetic photons at Triangle Universities Nuclear Laboratory (TUNL) in Durham, NC, USA. The excellent resolution of high-purity germanium (HPGe) detectors, that are used to detect the decay photons during the NRF measurements (for details see Sec. II), allow us to distinguish even close lying excited states.

The low-lying dipole strength of ^{94}Mo up to 4 MeV has been investigated comprehensively with various techniques of γ spectroscopy [38,39]. In these measurements low-spin collective excitations were studied. The present article focuses on the dipole strength in the PDR region and aims to answer the question whether an enhancement of electric dipole strength can be observed in the open-shell nucleus ^{94}Mo. The investigation of low-lying dipole strength in ^{94}Mo was also addressed by NRF measurements at the Helmholtz-Zentrum Dresden-Rossendorf [17,18]. However, the analysis of the experimental data was carried out in energy bins only and used statistical methods like Monte Carlo simulations of the γ decay. The present paper reports on a different approach for the analysis of the data from our new measurements; dipole strengths and spin quantum numbers are directly determined for the individual states. Furthermore, measurements with linearly polarized, quasi-monochromatic photon beams provide information on the parity quantum number of excited states and on their average decay pattern.

In the next section a short overview is given of the experimental setups and techniques used to investigate ^{94}Mo. The analysis of the data is briefly explained. In Sec. III the results of the measurements on ^{94}Mo are presented. Finally, the results are discussed in Sec. IV. The measured dipole-strength distribution is compared to calculations within the quasiparticle phonon model (QPM) [40]. Furthermore, the average decay pattern of the dipole excited states is analyzed and compared to results of simulations with the DICEBOX code [41].

II. EXPERIMENTAL SETUPS AND METHODS

The photoresponse of the isotope ^{94}Mo was investigated within two nuclear resonance fluorescence experiments: one using unpolarized bremsstrahlung with a continuous spectral distribution, and the other using quasi-monoenergetic, 100% linearly polarized photons from laser Compton backscattering (LCB) in the entrance channel.

The combination of measurements with continuous bremsstrahlung and quasi-monoenergetic, linearly polarized photons has been proven to be a powerful method for the comprehensive study of dipole excited states up to the neutron separation threshold. While NRF measurements with bremsstrahlung give an overview over the existing dipole states up to the endpoint energy, measurements with LCB γ rays allow a selective study of certain excited states. Combining both methods, it is possible to determine cross sections as well as spin and parity quantum numbers of the excited states in a model-independent way.

The experimental methods and the setups are introduced in this section. A more detailed description of the NRF method can be found in Refs. [9,10].

A. NRF at DHIPS

The photon-scattering experiment with bremsstrahlung was performed at the Darmstadt High Intensity Photon Setup (DHIPS) [42]. Bremsstrahlung is produced by stopping an electron beam in a thick copper radiator target. The electron beam is provided by the injector of the Superconducting Darmstadt Electron Linear Accelerator, S-DALINAC. The generated photon beam passes a large copper collimator and has a size of about 2.5 cm diameter at the NRF target position. Target nuclei are excited by the resonant absorption of photons and subsequent decay either directly or via intermediate states back to the ground state. In order to detect the scattered photons three high-purity germanium detectors with 100% efficiency relative to a standard $3'' \times 3''$ NaI detector at a γ-ray energy of 1.3 MeV are placed at 90° and 130° with respect to the incident beam. To suppress low-energy background radiation and Compton background, the detectors are shielded with lead and active anti-Compton shields made of bismuth germanate (BGO), respectively.

Two measurements on ^{94}Mo were performed with bremsstrahlung at endpoint energies of 7.65 and 8.70 MeV, respectively. For the measurement at 7.65 MeV the target consisted of 1 g molybdenum powder enriched to 94% in the isotope ^{94}Mo and 0.49 g enriched to 78%, resulting in a total ^{94}Mo mass of 1.32 g. In order to calibrate the energy and the photon flux, 0.87 g boron powder of natural isotopic composition was added (see below for details). In the second measurement at 8.70 MeV the target consisted of 0.88 g of Mo powder enriched to 98.97% in ^{94}Mo. As calibration standard 0.31 g of ^{11}B with a high isotopic purity of 99.52% was chosen. Each of the two measurements lasted about 115 h.

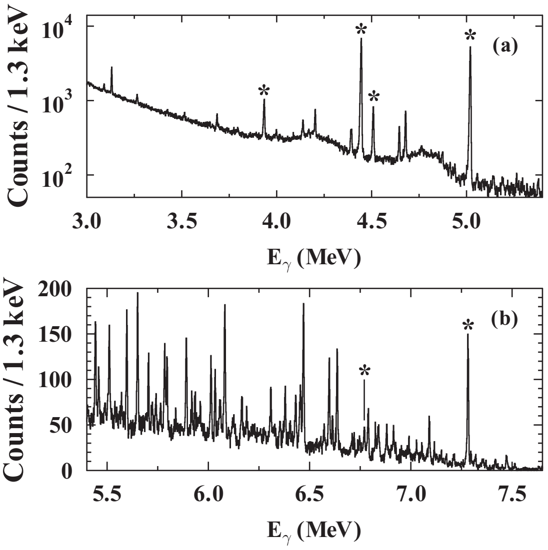

FIG. 1. Spectrum of ^{94}Mo measured at DHIPS with an endpoint energy of 7.65 MeV at 130° with respect to the incoming beam. The upper part (a) shows the region between 3 and 5.4 MeV on a logarithmic scale and the lower part (b) the region between 5.4 and 7.65 MeV on a linear scale. Peaks stemming from transitions of the calibration standard ^{11}B and corresponding escape lines are marked with an asterisk.

Figure 1 shows a spectrum in the energy range between 3 and 7.65 MeV measured with a detector placed at 130° with respect to the incident beam. The corresponding endpoint energy was 7.65 MeV. Most of the observed peaks can be assigned to decays of excited states of ^{94}Mo. Few peaks, marked with asterisks, stem from the calibration standard ^{11}B.

In NRF measurements the peak areas $A_{i,f}$ are directly proportional to the integrated cross section $I_{i,f}$ for the resonant absorption of photons by the ground state to an excited state i and the subsequent decay to a state f:

$$A_{i,f} = N_T I_{i,f} W(\vartheta)\Phi_\gamma(E_i)\epsilon(E_i - E_f). \tag{1}$$

Here, N_T is the number of target nuclei, $W(\vartheta)$ the angular distribution of the emitted photons, and Φ_γ the photon flux. The geometrical and intrinsic detector efficiencies are combined in $\epsilon(E)$. Furthermore, the integrated cross section $I_{i,0}$ for the direct decay to the ground state is connected to the ground-state transition width Γ_0:

$$I_{i,0} = \pi^2 \left(\frac{\hbar c}{E_i}\right)^2 g\frac{\Gamma_0^2}{\Gamma}. \tag{2}$$

In Eq. (2), Γ denotes the total decay width of the excited state with energy E_i. The statistical factor is given by $g = (2J_i + 1)/(2J_0 + 1)$ where J_i and J_0 are the spin quantum numbers of the excited and the ground state, respectively.

Since in NRF measurements mainly dipole and to a lesser extent quadrupole transitions are induced, only the spin sequences $0 \to 1 \to 0$ and $0 \to 2 \to 0$ occur for excitation from and decay back to the ground state for the case of an even-even nucleus. The ratio $W(\vartheta_1)/W(\vartheta_2)$ of the angular distributions at two different angles is a characteristic quantity for the spin sequences and, thus, allows the assignment of spin quantum numbers of excited states. At DHIPS the HPGe detectors are placed at 90° and 130° with respect to the incoming beam. For the above mentioned spin sequences the ratios are expected to be $W_{0\to1\to0}(90^\circ)/W_{0\to1\to0}(130^\circ) = 0.71$ and $W_{0\to2\to0}(90^\circ)/W_{0\to2\to0}(130^\circ) = 2.26$, respectively. Since the two ratios differ substantially, it is possible to assign a spin quantum number even to weakly excited states corresponding to poor statistics. Figure 2 shows the ratio $W(90^\circ)/W(130^\circ)$ for the observed ground-state transitions in the NRF measurements as a function of the excitation energy of the corresponding states. For most states spin $J = 1$ can be assigned unambiguously. The spin quantum number of the five lowest-lying states which were observed in the measurements at DHIPS (the ground-state transition of the level at 2739.6 keV was not observed in the measurement at 7.65 MeV endpoint energy) are already known [38,39]. The level at 871.0 keV is the 2_1^+ state of ^{94}Mo. The states at 2739.6, 3128.5, 3262.7, and 3512.0 keV are dipole excited states. However, only the ratio of the level at 3128.5 keV is, within the uncertainties, in agreement with 0.71, which is expected for a $J = 1$ state that is predominantly populated from the $J^\pi = 0^+$ ground state. For the other states, ratios close to unity have been measured. This indicates that the corresponding states were not only excited by the incoming beam but also fed from higher-lying states, diluting on average its photon-emission angular distribution.

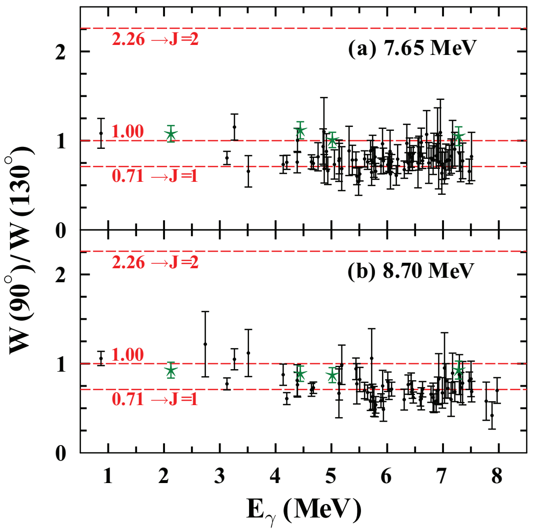

FIG. 2. (Color online) Experimentally determined values of the ratio $W(90^\circ)/W(130^\circ)$ for the ground-state transitions in ^{94}Mo observed in the NRF measurements at DHIPS. The upper (a) and lower (b) panels show the results for the measurement at 7.65 and 8.70 MeV endpoint energy, respectively. The green stars represent transitions in the calibration standard ^{11}B, which are expected to be nearly isotropic.

Finally, the transition strength $B(\lambda L)\uparrow$ for photo absorption, with λ being the radiation character (either electric or magnetic) and L being the order of the multipole radiation, can directly be calculated from the ground-state transition width,

$$\Gamma_0 = \frac{8\pi}{g}\sum_L \left(\frac{E_\gamma}{\hbar c}\right)^{2L+1} \frac{(L+1)}{L[(2L+1)!!]^2} B(\lambda L)\uparrow, \tag{3}$$

where E_γ is the photon energy.

For the calculation of $B(\lambda L)\uparrow$ the knowledge of absolute values for Γ_0 is necessary. However, as shown in Eq. (2), NRF measurements are sensitive to the product of Γ_0 with the branching ratio Γ_0/Γ to the ground state. The investigation of the photoresponse of isotopes at two (or more) different endpoint energies allows for the identification of decay branches to lower-lying excited levels.

In this work, for ^{94}Mo only for one state was a decay branch to a lower-lying state observed directly. In 19 cases the energy difference between two lines in the spectra coincides with the energy of lower-lying levels in ^{94}Mo (for further discussion see Sec. III). However, this is not sufficient to identify a decay via intermediate states and, consequently, in most cases no branching ratio can be deduced. Nevertheless, very weak branching ratios may be below the experimental sensitivity limit. Thus, the values for transition strengths given in this work have to be interpreted as lower limits for the true transition strengths that in most cases are expected to be very close to the given values.

B. NRF at HIγS

The High Intensity γ-Ray Source (HIγS) [43] is operated by the Triangle Universities Nuclear Laboratory and the Duke Free Electron Laser Laboratory (DFELL) at Duke University in Durham, NC, USA. It provides a quasi-monoenergetic, 100% linearly polarized γ-ray beam. Electrons are injected into the Duke/OK-4 storage ring free electron laser (FEL). The wiggler system in the storage ring forces the electron bunches onto sinusoidal trajectories resulting in the production of laser photons. After reflection inside the optical cavity, the laser photons are Compton backscattered from another electron bunch and, thus, boosted to higher energies. The wavelength of the FEL photons as well as the energy of the electrons can be tuned over a broad range. Hence, γ rays with energies between 1 and 100 MeV can be produced at HIγS. Since the process of Compton backscattering conserves the polarization of the FEL photons, the γ-ray beam generated at HIγS is fully linearly polarized [44].

The beam passes a collimator system approximately 60 m downstream of the collision point which selects a certain energy range of the γ rays produced in 180° Compton backscattering. For the NRF experiments on ^{94}Mo a collimator with 2.54 cm diameter was chosen resulting in an energy width of the photon-flux distribution corresponding to 3% of the mean photon energy.

The target used for the NRF experiments consisted of 2.89 g molybdenum powder enriched to 99% in ^{94}Mo. Five measurements were performed with mean beam energies of 5.47, 6.05, 6.44, 6.61, and 6.89 MeV. Each measurement lasted between three and four hours.

The target was centered between four HPGe detectors, each with 60% relative efficiency. The detectors are placed perpendicular (polar angle $\vartheta = 90^\circ$) to the incoming beam: two of them in the (horizontal) polarization plane at azimuthal angles $\varphi = 0^\circ$ and $\varphi = 180^\circ$ and two perpendicular to it at $\varphi = 90^\circ$ and $\varphi = 270^\circ$, respectively. The setup was optimized to measure the parity quantum number of excited states as described below.

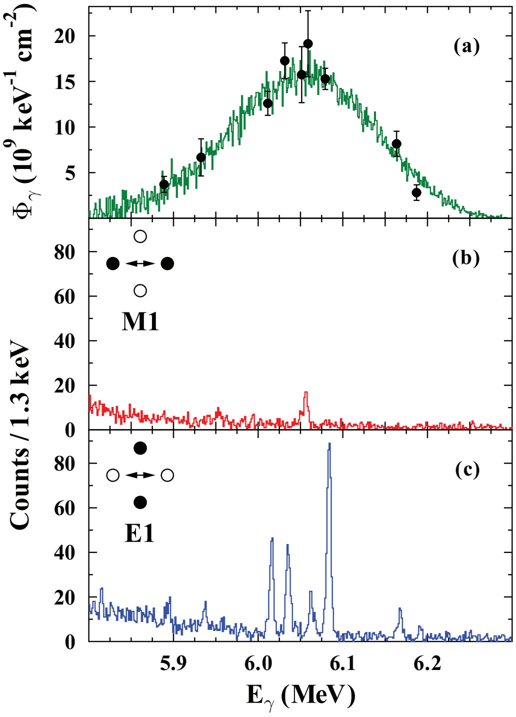

FIG. 3. (Color online) Spectra of ^{94}Mo recorded at HIγS at a centroid beam energy of 6.05 MeV. The photon-flux distribution (a) was measured with an in-beam detector before the actual measurement and corrected for detector response. Then, the distribution was scaled to experimental values for the photon flux represented by the black points. Spectrum (b) was recorded in the polarization plane, spectrum (c) perpendicular to it.

Figure 3 shows exemplary spectra measured in the polarization plane [Fig. 3(b)] and perpendicular to it [Fig. 3(c)]. The mean beam energy was 6.05 MeV. The narrow photon-flux distribution of the incoming beam is shown in Fig. 3(a). It was measured with an in-beam detector ($\vartheta = 0^\circ$) and corrected for the detector response which was determined using GEANT4 [45] simulations. Finally, the distribution was normalized to absolute values for the flux (black points). The latter were deduced exploiting the measured peak areas from the HIγS measurements in combination with the corresponding photon-scattering cross sections of ^{94}Mo that have been measured at DHIPS (see Sec. III).

Only within the narrow energy range of the photon-flux distribution are excited states populated from the ground state. Due to the large distance between the production spot of the LCB photons and the experimental setup the background is low, and even weakly excited states can be investigated.

The determination of the parity quantum number of an excited state requires information on the polarization of the γ rays either in the entrance or in the decay channel. The latter can be measured exploiting the method of Compton polarimetry. However, this method suffers from the low analyzing power of Compton polarimeters at energies above about 4 MeV. Higher photo-peak efficiencies, Compton polarimeters with higher granularity, and longer measuring times can make Compton polarimetry applicable [46–48]. However, the analysis power remains rather poor.

Alternatively, polarized γ rays in the entrance channel can be used [49]. The angular distribution of photons emitted after a $0^+ \xrightarrow{\vec{\gamma}} 1^\pi \xrightarrow{\gamma} 0^+$ spin sequence with $\pi = \pm 1$ representing the parity of the excited dipole state is given by

$$W(\vartheta, \varphi) = 1 + \tfrac{1}{4} P_2(\cos\vartheta) - \tfrac{1}{8}\pi \cos(2\varphi) P_2^{(2)}(\cos\vartheta). \quad (4)$$

In Eq. (4), ϑ denotes the polar scattering angle with respect to the incident γ-ray beam and φ denotes the azimuthal angle of the reaction plane with respect to the polarization plane of the incident beam. The unnormalized associated Legendre polynomial of second order is abbreviated by $P_2^{(2)}$.

According to Eq. (4) the angular distributions for $M1$ and $E1$ transitions exhibit maxima in and perpendicular to the polarization plane, respectivley. Therefore, in order to measure parity quantum numbers, at least two detectors are needed: one placed at $\vartheta = 90^\circ$ and $\varphi = 0^\circ$, as well as one at $\vartheta = 90^\circ$ and $\varphi = 90^\circ$. This geometry results in the highest analyzing power Σ:

$$\Sigma = \frac{W(90^\circ, 0^\circ) - W(90^\circ, 90^\circ)}{W(90^\circ, 0^\circ) + W(90^\circ, 90^\circ)} = \begin{cases} +1 & \text{for} \quad J = 1^+, \\ -1 & \text{for} \quad J = 1^-. \end{cases} \quad (5)$$

The high analyzing power allows the determination of parity quantum numbers even with low statistics. Finite-size effects of the HPGe detectors reduce the analyzing power slightly in the present geometry. The experimental observable is the so-called asymmetry ε, defined by the ratio of the measured and efficiency corrected peak intensities $A_\parallel$ in and $A_\perp$ perpendicular to the polarization plane:

$$\varepsilon = \frac{A_\parallel - A_\perp}{A_\parallel + A_\perp} = q\Sigma. \quad (6)$$

The asymmetry is given by the product of the analyzing power Σ and the experimental sensitivity q which accounts for finite opening angles of the detectors and the finite size of the target. It can be determined by means of a fit to the experimental data. For the setup realized in this experiment its value is $q = 0.93(1)$.

Figure 4 shows the experimental asymmetry ε for the ground-state transitions observed in the measurements at HIγS. An unambiguous assignment of the parity quantum number for each observed state was possible. In the investigated energy range all dipole excited states except one show negative parity.

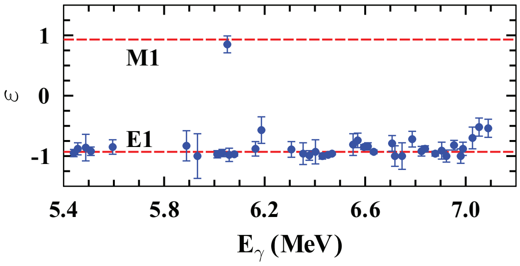

FIG. 4. (Color online) Experimental asymmetries for the ground-state transitions observed at HIγS. The expectation values for $E1$ and $M1$ transitions are indicated by the red dashed lines.

The results of the campaign are presented and discussed in the following chapters.

III. RESULTS

In total, 83 excited states of ^{94}Mo were observed in the energy range up to 8 MeV. The five lowest-lying states are already known from other measurements [38,39,50]. Ten excited states between 3.2 and 7.1 MeV have also been observed in an $(\alpha, \alpha'\gamma)$ experiment [51].

For 80 excited states the spin quantum number J was firmly determined. Except for the single $J = 2$ state observed at 871 keV excitation energy, all states have been assigned $J = 1$. Parity quantum numbers were determined for 41 of the excited dipole states (40 states with negative parity and one with positive parity). For all observed $J = 1$ states the product Γ_0^2/Γ was derived. The according transition strengths $B(E1)\uparrow$ and $B(M1)\uparrow$ for electric and magnetic dipole transitions, respectively, were obtained assuming $\Gamma_0/\Gamma = 1$. However, in two cases, which will be discussed at the end of this section, a branching transition to the 2_1^+ level has been taken into account. The results are listed in Tables I and II.

Table I gives the results for the five states of ^{94}Mo at lowest energies observed in this work in comparison with results published by Fransen *et al.* [39] that were obtained from previous NRF measurements at endpoint energies of 3.3 and 4 MeV [38]. Within the uncertainties the level energies found in this work are in good agreement with those given in Ref. [39]. Only for the excited state at 3261.7(2) keV is a slightly smaller energy of 3260.8(5) keV reported in Ref. [39].

In agreement with Ref. [39] the spin quantum number of the excited states at 3128.5 and 3512.0 keV was determined as $J = 1$. A spin assignment to the remaining three states was not possible within the uncertainties of the ratio $W(90^\circ)/W(130^\circ)$.

The values for the product Γ_0^2/Γ in the last column are calculated from the lifetime τ of the excited states and the relative intensities given in Ref. [39]. The corresponding results for $\langle\Gamma_0^2/\Gamma\rangle_{\text{eff}}$ obtained in the present work are considerably larger for the measurement with an endpoint energy of 8.7 MeV, because the low-lying states are not only excited from the ground state, but also fed by the decay of higher-lying states. Only the transition width of the excited state at 3512.0 keV is considerably smaller than reported in Ref. [39]. However, the value given in Ref. [39] has a large uncertainty. While the 2_1^+ level is strongly fed in both measurements, at 7.65 and 8.7 MeV endpoint energies, the states at 3128.5 and 3261.7 keV exhibit feeding only for the 8.7 MeV measurement. The level at 3512.0 keV exhibits no feeding at all. Apparently, the feeding increases with increasing number of states populated in the measurement. This observation is also reported for other nuclei [24,26].

Data on the remaining 78 higher-lying states are summarized in Table II. Without any exception they have spin quantum number $J = 1$. If known, also the parity quantum number π is given. The product Γ_0^2/Γ and either the $B(E1)\uparrow$ or the $B(M1)\uparrow$ transition strengths are listed.

TABLE I. The five lowest-lying excited states of ^{94}Mo observed in this work. The deduced level energies E_{level}, spin quantum numbers J, and the product Γ_0^2/Γ are compared with results of former NRF measurements by Fransen *et al.* [39] at 3.3 and 4 MeV endpoint energies.

	This experiment				Taken from Ref. [39]		
	7.65 MeV		8.7 MeV		3.3 and 4 MeV		
E_{Level} (keV)	J_j^π ($\hbar$)	$\langle\frac{\Gamma_0^2}{\Gamma}\rangle_{\mathrm{eff}}$ (meV)	J_j^π ($\hbar$)	$\langle\frac{\Gamma_0^2}{\Gamma}\rangle_{\mathrm{eff}}$ (meV)	E_{Level} (keV)	J_j^π ($\hbar$)	$\frac{\Gamma_0^2}{\Gamma}$ (meV)
871.0(1)		0.8(3)		3.1(12)	871.09(10)	2_1^+	0.165(4)[b]
2739.6(4)[a]				7(2)	2739.9(1)	1_1^+	0.93(30)
3128.5(1)	1	54(4)	1	71(7)	3128.6(2)	1_2^+	46(3)
3261.7(2)		11(2)		20(5)	3260.8(5)	1_1^-	11.5(12)
3512.0(2)	1	6.7(9)	(1)	10.8(28)	3511.7(2)	$1_3^{(+)}$	$12.8^{+6.0}_{-5.5}$

[a] Only observed in the measurement at 8.7 MeV endpoint energy.

[b] Taken from Ref. [50].

For the measurements with endpoint energies of 7.65 and 8.70 MeV, respectively, different targets have been used. The resulting transition strengths agree on average within 20%. Thus, all given values beside the spin quantum number are, if available, weighted average values of both measurements. In addition to the given statistical uncertainties for the product Γ_0^2/Γ and the transition strengths $B(E1)\uparrow$ and $B(M1)\uparrow$ in Table II, a systematic uncertainty of 20% has to be taken into account.

The observed feeding of the low-lying levels suggests that higher-lying excited states do not only decay directly to the ground state, but also via intermediate states. As mentioned in Sec. II A, applying the Ritz variation principle, the energy difference between two γ-ray transitions with energies $E_{\gamma,1}$ and $E_{\gamma,2}$ can be investigated to search for possible decays to intermediate states. If the energy difference is in accordance with the energy of a low-lying state, e.g., the 2_1^+ state, the level at $E_{\gamma,1}$ could decay via this state, resulting in a so-called inelastic scattering peak at $E_{\gamma,2}$. Here, in analogy to classical scattering experiments, inelastic means that one of the scattering bodies remains in an excited state after collision. On the other hand, the term elastic denotes the direct decay to the ground state.

For the following analysis the list of peak energies was extended by the 12 lowest-lying states (only 0^+, $1^\pm$, 2^+, and $3^\pm$ states) up to 3 MeV of ^{94}Mo which were not observed in this measurement. Nevertheless, they could be fed by higher levels, but not be observed due to too high background at lower energies. All combinations of peak energies in this list were compared with those level energies. In total, 19 energy differences were found that coincide with a level energy within ±1 keV. As an example, the seven peaks that could stem from decays to the 2_1^+ level, are summarized in Table III. Please note that four (five) energy differences are found to coincide with randomly chosen energies of 810.5 keV (925.4 keV) for the 2_1^+ level.

The first pair of peaks at $E_{\gamma,1} = 4136.0$ keV and $E_{\gamma,2} = 3265.2$ keV can be assigned as the elastic and inelastic decay of the level at $E_{\mathrm{x}} = E_{\gamma,1}$ to the ground state and to the 2_1^+ state, respectively. Reference [39] reports on a (γ,γ') measurement on ^{94}Mo with an endpoint energy of 4.0 MeV. Thus, the level at 4136.0 keV was not excited. In this measurement no peak at 3265.2 keV was observed. In an $(\alpha,\alpha'\gamma)$ measurement on ^{94}Mo [51] the decay of the level at 4136.0 keV to the 2_1^+ state was observed. The branching ratio was reported as $\Gamma_{2_1^+}/\Gamma = 0.53(4)$ in Ref. [51]. In the present measurement it was determined to $\Gamma_{2_1^+}/\Gamma = 0.36(3)$. For the calculation of the $B(E1)\uparrow$ and the $B(M1)\uparrow$ strengths the corresponding branching ratio $\Gamma_0/\Gamma = 0.64(4)$ to the ground state was used (see Table II).

In two other cases, branching ratios to the 2_1^+ level were observed in the $(\alpha,\alpha'\gamma)$ measurement [51]. For the excited states at 5440.5 and 5702.1 keV the branching ratios are given as $\Gamma_{2_1^+}/\Gamma = 0.45(6)$ and $\Gamma_{2_1^+}/\Gamma = 0.27(3)$, respectively. However, in the present measurements no peaks were observed at the corresponding energies 4569.5 and 4831.1 keV. From the sensitivity limit of our data upper limits for the branching ratios were determined to be $\Gamma_{2_1^+}/\Gamma < 0.19$ and $\Gamma_{2_1^+}/\Gamma < 0.28$. The latter one is in agreement with the result of the $(\alpha,\alpha'\gamma)$ measurement. As marked in Table II, the branching ratio to the ground state for the level at 5702.1 keV was taken from Ref. [51] to derive the excitation strength.

No inelastic character can be assigned to the peaks at 6051.4 and 6904.4 keV as listed in Table III. The peak at 6051.4 keV is also observed in the measurements at HIγS. Since the range of excitation was only about 300 keV wide, it has to stem from a transition to the ground state of ^{94}Mo. The same holds for the peak at 6904.4 keV. The level at 7775.4 keV, which might decay to the 2_1^+ level resulting in a peak at 6904.4 keV, is only excited in the measurement with an endpoint energy of 8.70 MeV. Nevertheless, the peak at 6904.4 keV is also observed in the measurement with lower endpoint.

These two examples and the coincidences of energy differences with randomly chosen level energies for the 2_1^+ level show that the energy information together with the Ritz variation principle cannot be considered as a sufficient identification of an inelastic transition. Consequently, for the remaining cases also no inelastic character was assigned.

Figure 5 shows the measured $B(E1)\uparrow$-strength distribution as a function of the excitation energy. Green bars (open circles) represent dipole transitions with firmly assigned electric character (see also Fig. 4). For the dipole transitions

TABLE II. Observed excited states of ^{94}Mo with their level energies E_{Level}, as well as spin (J) and parity (π) quantum numbers. Results for Γ_0^2/Γ and, depending on J^π, either the $B(E1)\uparrow$ or the $B(M1)\uparrow$ transition strength are listed. The given numbers are the weighted average of the NRF measurements at DHIPS.

E_{Level} (keV)	J^π	$\frac{\Gamma_0^2}{\Gamma}$ (meV)	$B(E1)_\uparrow$ ($10^{-3}\ e^2\mathrm{fm}^2$)	$B(M1)_\uparrow$ ($10^{-3}\mu_N^2$)	E_{Level} (keV)	J^π	$\frac{\Gamma_0^2}{\Gamma}$ (meV)	$B(E1)_\uparrow$ ($10^{-3}\ e^2\mathrm{fm}^2$)	$B(M1)_\uparrow$ ($10^{-3}\mu_N^2$)
4136.0(2)	1	34(3)	2.16(23)[a]	195(21)[a]	6306.4(4)	1^-	115(7)	1.31(8)	
4200.6(1)	1	67(3)	2.59(12)	234(10)	6353.0(5)	1^-	59(6)	0.66(7)	
4387.5(2)	1	30(3)	1.02(10)	92(9)	6377.6(2)	1^-	151(14)	1.67(15)	
4392.2(2)	1	39(4)	1.32(14)	119(12)	6402.1(6)	1^-	58(7)	0.63(8)	
4643.7(1)	1	86(10)	2.46(29)	223(25)	6429.6(2)	1^-	151(9)	1.63(10)	
4677.0(2)	1	167(16)	4.68(45)	423(40)	6452.5(2)	1^-	184(10)	1.96(11)	
4761.5(3)[b]	1	21(2)	0.56(5)	50(5)	6468.1(1)	1^-	423(19)	4.48(20)	
4851.9(3)[b]	1	19(2)	0.48(5)	43(4)	6551.9(6)	1^-	41(7)	0.42(7)	
4865.4(8)[b]	1	15(3)	0.37(7)	34(7)	6570.2(4)	1^-	72(7)	0.73(7)	
4871.9(4)[b]	1	22(3)	0.55(7)	49(7)	6595.1(1)	1^-	327(17)	3.27(17)	
4910.6(4)[b]	1	18(2)	0.44(5)	39(4)	6610.8(3)	1^-	135(9)	1.34(9)	
4936.6(5)[b]	1	17(2)	0.41(5)	37(4)	6634.1(2)	1^-	352(17)	3.46(17)	
5054.1(4)[b]	1	16(2)	0.36(4)	32(4)	6707.1(6)	1^-	75(9)	0.71(9)	
5137.2(8)	1	15(2)	0.32(4)	29(4)	6718.3(5)	1^-	68(10)	0.64(9)	
5141.8(5)	1	28(3)	0.59(6)	53(6)	6746.7(5)	1^-	82(9)	0.77(8)	
5186.2(5)	1	18(6)	0.37(12)	33(11)	6787.1(5)	1^-	249(14)	2.28(13)	
5316.8(6)	1	13(2)	0.25(4)	22(3)	6824.0(4)	1^-	125(10)	1.13(9)	
5375.9(4)	1	22(2)	0.41(4)	37(3)	6838.3(2)	1^-	202(13)	1.81(12)	
5440.5(1)	1^-	98(8)	1.74(14)		6878.9(3)	1^-	178(12)	1.57(11)	
5456.5(5)	1^-	40(4)	0.71(7)		6904.4(5)	1^-	96(20)	0.84(17)	
5488.2(4)	1^-	21(4)	0.36(7)		6923.2(5)	1^-	71(9)	0.61(8)	
5508.5(2)	1^-	86(6)	1.47(10)		6953.5(5)	1^-	61(8)	0.52(7)	
5595.3(1)	1^-	113(6)	1.85(10)		6980.1(7)	1^-	49(8)	0.41(7)	
5648.6(1)	1	135(7)	2.15(11)	194(10)	6989.1(7)	1^-	122(10)	1.02(8)	
5702.1(2)	1	79(5)	1.67(13)[c]	151(11)[c]	7027.0(5)	1^-	85(15)	0.70(12)	
5720.4(9)	1	30(3)	0.46(5)	42(4)	7053.1(7)	1^-	124(11)	1.01(9)	
5739.1(2)	1	47(6)	0.71(9)	64(8)	7089.5(2)	1^-	369(22)	2.97(18)	
5762.3(4)	1	35(5)	0.52(7)	47(7)	7147.6(7)	1	128(12)	1.00(9)	91(8)
5782.4(1)	1	99(7)	1.47(10)	133(9)	7172.2(4)	1	123(12)	0.96(9)	86(8)
5793.8(1)	1	88(8)	1.30(12)	117(10)	7211.9(4)	1	222(36)	1.70(28)	154(24)
5888.9(1)	1^-	128(11)	1.80(15)		7294.5(5)	1	182(19)	1.34(14)	122(12)
5932.6(2)	1^-	57(7)	0.78(10)		7316.9(3)	1	190(16)	1.39(12)	126(10)
6011.4(3)	1^-	134(9)	1.77(12)		7351.3(6)	1	135(14)	0.97(10)	88(9)
6031.5(2)	1^-	111(9)	1.45(12)		7471.9(2)	1	481(34)	3.31(23)	299(21)
6051.4(7)	1^+	46(6)		54(7)	7503.4(7)	1	215(26)	1.46(18)	132(16)
6058.9(5)	1^-	43(6)	0.55(8)		7513.8(4)	1	283(50)	1.91(34)	173(30)
6079.3(1)	1^-	260(14)	3.32(18)		7775.4(8)	1	144(23)	0.88(14)	79(12)
6163.5(4)	1^-	76(7)	0.93(9)		7879.2(8)	1	186(50)	1.09(29)	99(26)
6187.1(3)	1^-	65(8)	0.79(10)		7971.8(21)	1	326(34)	1.85(19)	167(17)

[a] Calculated with $\Gamma_0/\Gamma = 0.64(4)$.
[b] Only observed in the measurement at 7.65 MeV endpoint energy.
[c] Calculated with $\Gamma_0/\Gamma = 0.73(3)$ from Ref. [51].

marked in red (black diamonds) electric character is assumed but not experimentally confirmed. The sensitivity limit of the experimental setup is represented by the grey solid line. Transitions weaker than the sensitivity limit cannot be observed.

IV. DISCUSSION

In this section the results presented in Sec. III are further discussed with respect to different properties.

A. QPM calculation

The quasiparticle phonon model [40] has been successfully used in the past to describe the fragmentation of the dipole strength below the threshold in different medium and heavy semimagic nuclei. Therefore, a QPM calculation was performed for the case of ^{94}Mo. For details of the model and the calculations see, e.g., Ref. [19]. Calculations for ^{94}Mo have been performed using a basis which includes one-, two-, and three-phonon configurations. While all 1^-

TABLE III. Energy differences of two γ-ray transitions at $E_{\gamma,1}$ and $E_{\gamma,2}$. Differences are listed if they are in accordance with the energy of the 2_1^+ level [$E_{2_1^+} = 871.0(1)$ keV] within ±1 keV.

$E_{\gamma,1}$ (keV)	$E_{\gamma,2}$ (keV)	$E_{\gamma,1} - E_{\gamma,2}$ (keV)
4136.0(2)	3265.2(3)	870.8(4)
5782.4(1)	4910.6(4)	871.8(4)
6187.1(3)	5316.8(6)	870.3(7)
6610.8(3)	5739.1(2)	871.7(4)
6634.1(2)	5762.3(4)	871.8(4)
6923.2(5)	6051.4(7)	871.8(9)
7775.4(8)	6904.4(5)	871.0(9)

one-phonon components (including the GDR) have been accounted for, two-phonon and three-phonon configurations have been truncated at 9 and 10 MeV, respectively. Complex components are built up of phonons with multipolarity from $1^{\pm}$ to $7^{\pm}$. For the $E1$ operator standard effective charges, e_π and e_ν, have been used to exclude the center of mass motion: $e_\pi = N/A$ for protons and $e_\nu = -Z/A$ for neutrons where N, Z, and A are the neutron, proton, and mass numbers, respectively.

Figure 6 shows a comparison between the experimentally determined $B(E1)\uparrow$-strength distribution and the results of the QPM calculation. Here, all observed dipole excited states, except firmly assigned 1^+ states, are assumed to have negative parity. However, since recently in a study of ^{90}Zr considerable $M1$ strength was observed above 7 MeV [52], magnetic character may not completely be excluded for the dipole states above about 7 MeV.

For easier comparison, the strength distributions were folded with a Lorentzian function with 200 keV width. Up to the endpoint energy at 8.70 MeV the convoluted distributions (red curves) show a good agreement between the experimental findings and the QPM.

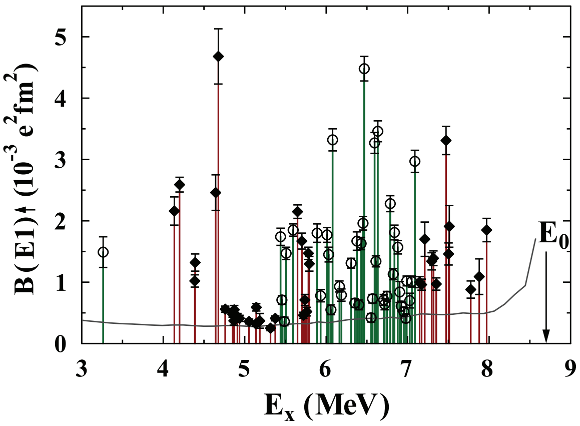

FIG. 5. (Color online) Experimentally determined $B(E1)\uparrow$-strength distribution of ^{94}Mo. For the dipole transitions marked with red bars (black diamonds) electric character is assumed. The electric character of the dipole excited states shown in green (open circles) is experimentally confirmed. The endpoint energy of the measurement at 8.70 MeV is marked by E_0. The sensitivity limit of the experimental setup is given by the grey curve.

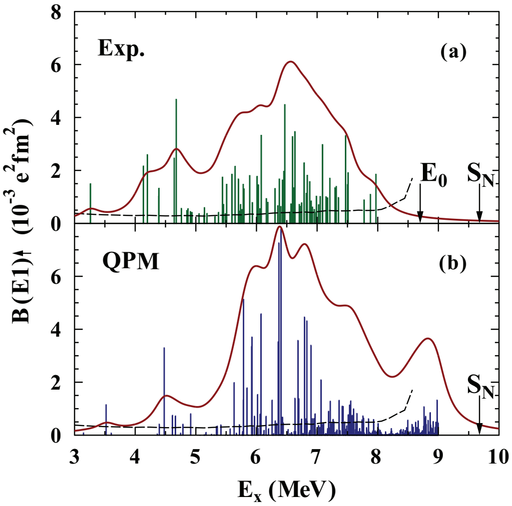

FIG. 6. (Color online) $B(E1)\uparrow$-strength distributions of ^{94}Mo: (a) Experimentally deduced strength distribution assuming all excited dipole states (except those with firmly assigned positive parity) have negative parity. (b) $E1$-strength distribution as calculated within the QPM up to 9 MeV. The endpoint energy of the experiment is marked by E_0 and the neutron separation energy by S_N. The experimental sensitivity limit is given by the grey curve. The red curves represent the strength distributions folded with a Lorentzian function with 200 keV width.

Diagonalization of the model Hamiltonian yields 219 (443) 1^- states below 8 (9) MeV. The summed $E1$-excitation strength obtained within the QPM between 5 and 8 MeV is $\sum B(E1)\uparrow = 106 \times 10^{-3}$ e^2fm^2. However, as shown in Ref. [29], for a correct comparison between calculation and experimental data, the sensitivity limit of the experiment has to be properly accounted for. In total, 66 of the QPM 1^- states below 8 MeV are calculated to show ground-state excitation strengths above the experimental sensitivity. Including only these states above the experimental limit, the total strength amounts to 91×10^{-3} e^2fm^2 for the QPM calculation.

In the experiment 78 dipole states were observed up to 8 MeV. Including the levels for which the radiation character is not experimentally confirmed, the sum of the measured $B(E1)\uparrow$ strengths in the energy range between 5 and 8 MeV results in $86(8) \times 10^{-3}$ e^2fm^2, which corresponds to 0.16(1)% of the TRK sum rule [2].

As shown in Ref. [29], the fragmentation of the $E1$ strength represents an observable to investigate whether the damping in the microscopic calculation is properly accounted for. Figure 7 shows the fragmentation of the $B(E1)\uparrow$ strength following the procedure outlined in Refs. [29,30]. The individual levels are grouped according to their $B(E1)\uparrow$ value in bins of 0.5×10^{-3} e^2fm^2. The strength of all levels in such a bin is summed up for each bin. These sum strengths $\sum B(E1)\uparrow$ are then plotted as a function of the strength of the individual states of the corresponding bin. Despite two rather strong transitions, the QPM calculation describes the data for states with $B(E1)\uparrow \gtrsim 1 \times 10^{-3}$ e^2fm^2 in a satisfactory manner.

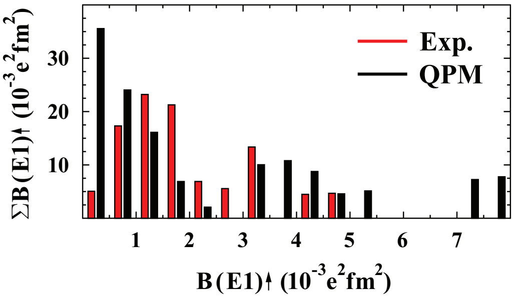

FIG. 7. (Color online) Fragmentation of the $B(E1)\uparrow$ strength. The experimental data are plotted with red bars, the QPM calculation with black bars. The strength is summed up in $0.5 \times 10^{-3}\ e^2\text{fm}^2$ wide bins and plotted as a function of the $B(E1)\uparrow$ strength bins.

The calculation predicts a significant amount of strength accumulated in weak transitions, which are not observed in the present experiment due to the limited sensitivity for $E1$ strength below $1 \times 10^{-3}\ e^2\text{fm}^2$.

In conclusion, the QPM calculation reproduces the experimental results well. It is in agreement with the total strength measured in the PDR region and also describes the strength distribution well. Furthermore, the fragmentation of the strength is reproduced. Thus, as already observed in Ref. [29], the QPM seems to properly treat the damping mechanism of the PDR which is included in the model as coupling to complex configurations.

B. $M1$ strength

The three lowest-lying $J^\pi = 1^+$ states at 2739.6, 3128.5, and 3512.0 keV (see Table I) observed in this work are already known. They are identified to be fragments of the $[2_1^+ \otimes 2_{\text{ms}}^+]_{1^+}$ two-phonon coupling [53,54] with the 3128.5 keV level being the main fragment [38,39].

Among the 41 states for which the parity quantum number was determined within this work one state was found to have positive parity. The level is located at 6051.4(7) keV. Its transition strength is determined as $B(M1)\uparrow = 54(7) \times 10^{-3}\mu_N^2$. Between approximately 5.9 and 7.1 MeV it is the only state that is excited by an $M1$ transition above the experimental sensitivity limit. The QPM calculations predict only very weak 1^+ states below 8 MeV as well. They allow also qualitative statements concerning the dominant contributions to the $M1$ strength. In accordance with the observations for ^{90}Zr in Ref. [52], our QPM calculations show that the $M1$ strength in the case of ^{94}Mo is generated via $\nu(g_{9/2}) \rightarrow \nu(g_{7/2})$ neutron spin-flip configurations. However, since in contrast to ^{90}Zr the $\pi(g_{9/2})$ shell is occupied with two protons in ^{94}Mo, they show that also $\pi(g_{9/2}) \rightarrow \pi(g_{7/2})$ proton spin-flip transitions contribute to the $M1$ strength.

C. Decay pattern

Most of the $B(E1)\uparrow$ strengths in Table II were determined assuming $\Gamma_0/\Gamma = 1$. This assumption is based on the fact that in the measurements only one transition to a lower-lying excited state was observed. However, the low-lying states are strongly fed (see Sec. III). Since there are no individual excited states, which significantly feed the low-lying levels, they have to be populated via several excited states with small branching ratios to the low-lying states.

As demonstrated in Ref. [55], the measurements at HIγS offer the opportunity to further study the average decay pattern of excited states. At HIγS states are excited in a narrow energy range only (see Sec. II B and Fig. 3) with a width smaller than the excitation energy $E_{2_1^+} = 871$ keV of the first excited state of ^{94}Mo. Peaks observed in this excitation range, thus, can unambiguously be identified as ground-state transitions. However, at low γ-ray energies the transition of the 2_1^+ state to the ground state with an energy of 871 keV is observed. Since the 2_1^+ level cannot be directly excited by the incoming photon beam, it has to be populated in the decay of states excited in the narrow energy range covered by the incoming photon beam. Decays of other low-lying states are not observed, i.e., they are not or only weakly fed. No peaks corresponding to direct decays of the $J = 1$ states to the 2_1^+ could be observed. Thus, no individual branching ratio of these states to the ground state and the 2_1^+ level can be deduced. However, some average features can be studied with help of the HIγS measurements: the azimuthal asymmetry of the angular distribution of the decay of the 2_1^+ level, its population yield, and a mean branching ratio to the ground state.

1. *Feeding of 2_1^+ level*

The asymmetry ε [as defined by Eq. (6)] of the distribution of the photons emitted in the decay of the 2_1^+ level can provide information on the decay pattern of the states that have been excited by the photon beam. Apart from a single 1^+ level, 1^- states were observed in the HIγS measurements exclusively. The excitation of states with spin $J = 2$ is strongly suppressed with respect to the excitation of $J = 1$ states. Thus, in the following, the 2_1^+ level is assumed to be fed in two ways only. It is either populated directly via one of the excited dipole states within a $0_{\text{gs}}^+ \rightarrow 1^- \rightarrow 2_1^+$ spin sequence, or it is populated via intermediate states: $0_{\text{gs}}^+ \rightarrow 1^- \rightarrow J_i^\pi \rightarrow J_j^\pi \rightarrow \cdots \rightarrow 2_1^+$. Assuming that the 2_1^+ state is exclusively fed via direct decays of 1^- states, the asymmetry with the present setup is $\varepsilon_{1^-} = 0.27$. On the other hand, when it is fed via intermediate states only, the angular distribution of the decay photons approaches isotropy. In the limit of many intermediate states involved in the γ cascade, the asymmetry vanishes: $\varepsilon_{\text{iso}} = 0$.

Figure 8 shows the experimentally deduced asymmetries $\varepsilon_{2_1^+}$ for each energy setting used at HIγS. The according uncertainties are rather large due to the low peak-to-background ratio at low energies. Nevertheless, different asymmetries of the decay of the 2_1^+ level were measured with the five energy settings. This may indicate varying decay patterns of the excited states in the different energy ranges.

In the energy range around 5.5 MeV the decay via intermediate states seems to dominate. At 6.05 MeV this picture completely changes and the direct decay to the 2_1^+ level is favored. For the higher energies rather large contributions of direct decays were observed as well. This suggests a different

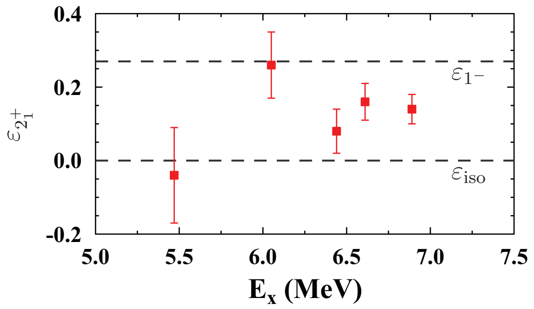

FIG. 8. (Color online) The experimental asymmetry of the decay photons of the 2_1^+ state at the five energy settings used in the HIγS measurements. The asymmetry is given by $\varepsilon_{1^-} = 0.27$, when the 2_1^+ state is exclusively fed via direct decays of 1^- states. For feeding via γ cascades through many intermediate states the asymmetry results in $\varepsilon_{\text{iso}} = 0$.

decay behavior of the 1^- states in the energy range between 6 and 7 MeV to those near 5.5 MeV.

2. *Cross sections*

In addition, it is also possible to extract the elastic cross section $\sigma_{\gamma\gamma}$, as well as the inelastic cross section $\sigma_{\gamma\gamma'}$ for each energy setting from the HIγS spectra. Here, as defined earlier, elastic means that the excited states decay directly back to the ground state. In contrast, the inelastic cross section is a measure for the decay via intermediate states. The total cross section is given by $\sigma_\gamma = \sigma_{\gamma\gamma} + \sigma_{\gamma\gamma'}$.

The elastic cross section $\sigma_{\gamma\gamma}$ is defined via

$$\sigma_{\gamma\gamma} = \frac{1}{N_T \Phi_\gamma^{\text{tot}}} \sum_i \frac{A_{i\to\text{gs}}}{\epsilon_{i\to\text{gs}} W_{i\to\text{gs}}(\vartheta,\varphi)}, \tag{7}$$

where the sum accounts for all resolved peak intensities $A_{i\to\text{gs}}$ corresponding to ground-state transitions from the levels excited by the γ-ray beam. The total photon flux was calculated via $\Phi_\gamma^{\text{tot}} = \int_0^\infty \Phi_\gamma(E)dE$. The photon-flux distribution $\Phi_\gamma(E)$ for each energy setting was determined as described in Sec. II B. The efficiency was calibrated with help of a ^{56}Co source and GEANT4 [45] simulations of the detector response. Finally, the angular distribution was determined with Eq. (4). Since the incoming γ-ray beam excited dipole states exclusively, Eq. (7) can be written as

$$\sigma_{\gamma\gamma} = \frac{1}{N_T \Phi_\gamma^{\text{tot}} W_{1\to\text{gs}}(\vartheta,\varphi)} \sum_i \frac{A_{i\to\text{gs}}}{\epsilon_{i\to\text{gs}}}. \tag{8}$$

In analogy to the elastic cross section, the expression for the inelastic cross section is given by

$$\sigma_{\gamma\gamma'} = \frac{1}{N_T \Phi_\gamma^{\text{tot}}} \sum_i \frac{A_{i\to\text{j}}}{\epsilon_{i\to j} W_{i\to j}(\vartheta,\varphi)}. \tag{9}$$

Here, the sum considers all transitions from all excited states i to states j except for the ground state. Therefore, it accounts for all inelastic decays. In addition to the ground-state decays, the decay of the 2_1^+ level was observed only. Thus, we assume that all states, which do not decay directly back to the ground state, decay either directly or via intermediate states to the 2_1^+ state. With this assumption, the peak area $A_{2_1^+\to\text{gs}}$ corresponding to the ground-state decay of the 2_1^+ level is an approximate measure for the integrated inelastic cross section and Eq. (9) can be expressed as

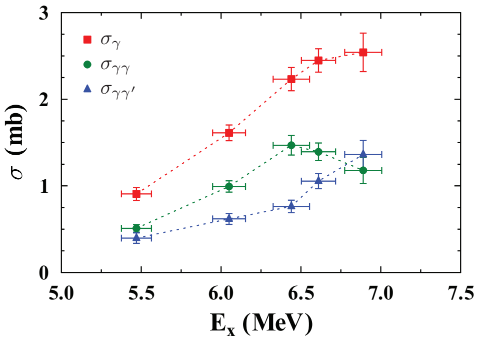

FIG. 9. (Color online) The total (red squares), elastic (green circles), and inelastic (blue triangles) cross sections measured at the five beam settings at HIγS.

$$\sigma_{\gamma\gamma'} \approx \frac{A_{2_1^+\to\text{gs}}}{N_T \Phi_\gamma^{\text{tot}} \epsilon_{2_1^+\to\text{gs}} W_{2_1^+\to\text{gs}}(\vartheta,\varphi)}. \tag{10}$$

In the previous section it was shown that the way in which the 2_1^+ level is populated, changes with energy. Thus, the angular distribution $W_{2_1^+\to\text{gs}}(\vartheta,\varphi)$ for the decay photons of the 2_1^+ state is different for each energy setting and has to be determined individually. Again assuming that there are only two mechanisms feeding the 2_1^+ level, either via direct decay of $J^\pi = 1^-$ states or via γ cascades, the asymmetry $\varepsilon_{2_1^+}$ can be used to determine the fraction of each way of feeding. Then, the effective angular distribution for the decay of the 2_1^+ level to the ground state is a superposition of the distributions after pure feeding via direct decays or γ cascades, respectively, weighted by the according fractions.

The observed elastic ($\sigma_{\gamma\gamma}$), inelastic ($\sigma_{\gamma\gamma'}$), and total (σ_γ) cross sections are plotted in Fig. 9 as a function of the excitation energy. The total cross section σ_γ smoothly increases with energy and flattens at higher energies. The flattening is due to the elastic cross section $\sigma_{\gamma\gamma}$ which drops above 6.5 MeV. Due to the increasing level density at higher energies the inelastic cross section strongly increases at energies higher than 6.4 MeV. Similar to the $B(E1)\uparrow$-strength distribution plotted in Fig. 6, the elastic cross section reveals a maximum at about 6.4 MeV.

An NRF measurement on ^{94}Mo was also performed at the Helmholtz-Zentrum Dresden-Rossendorf in Dresden, Germany [17]. In this experiment bremsstrahlung photons with an endpoint energy of 13.2 MeV were used in the entrance channel. The analysis of the data was carried out in a different manner than discussed in this paper. First, the measured spectra were corrected for the detector response and the background stemming from atomic scattering. The detector response, as well as the atomic background were obtained from Monte Carlo simulations. The remaining part of the spectrum was considered as the full intensity of the ground-state transitions,

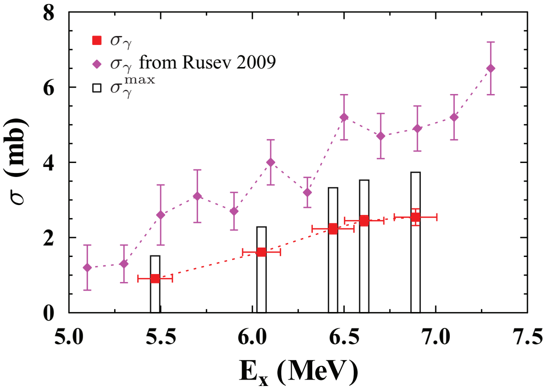

FIG. 10. (Color online) Comparison of total cross section up to 7.5 MeV deduced in this work (red squares) and determined in Ref. [17] (Rusev 2009, magenta diamonds). A comparison to (γ, n) data is reported in Ref. [17]. The height of the gray bars represents an upper limit for the total cross section extracted from our measurements at HIγS (see text for details).

including the individual peaks and also a continuum of so-called unresolved strength. That spectrum was analyzed in 200 keV wide energy bins. Furthermore, the resulting values for the cross section were corrected for feeding and branching effects with help of simulations of γ cascades within the statistical model.

Figure 10 shows a comparison of the total cross section as obtained in this work (red squares) and as determined in Ref. [17] (magenta diamonds). Obviously, the cross sections from Ref. [17] are considerably larger than the cross sections from this work. This discrepancy may be attributed to two reasons. Using simulations of γ cascades, the cross section was corrected for all possible feeding and branching effects in Ref. [17]. However, in the present analysis we assume that all states decaying via intermediate states, decay via the 2_1^+ level. Thus, inelastic decays that do not decay via the 2_1^+ state are not taken into account and the inelastic part $\sigma_{\gamma\gamma'}$ of the cross section is underestimated. However, the fraction of inelastic decays decaying not via the 2_1^+ level is usually rather small. For example, the 2^+ levels of ^{94}Mo below 3 MeV have only small branching ratios to the ground state (smaller than 13% for the worst case of the 2_3^+ level at 2067.35 keV excitation energy) while the decay via the 2_1^+ level dominates. This is also supported by calculations within the statistical model, which will be discussed in the next section. They show that for the HIγS measurement at 5.47 MeV only about 12% and for the measurement at 6.89 MeV about 18% of all inelastic decays occur not via the 2_1^+ level.

On the other hand, since only individual peaks are taken into account for the elastic decay channel to stay independent of simulations, unresolved strength is not accounted for in the present analysis. To quantify the maximum influence of unresolved strength to the total cross section in ^{94}Mo, an upper limit $\sigma_{\gamma\gamma}^{\max}$ for the elastic cross section was extracted from the spectra measured at HIγS: The limit was deduced by integrating the total (efficiency corrected) intensity in the spectra within an energy interval of ±100 keV around the mean beam energy E_{mean}. The width of the energy interval for integration of the entire spectrum was chosen to match the 200 keV-bin size used in the analysis of Ref. [17]. In analogy to Eq. (8), $\sigma_{\gamma\gamma}^{\max}$ was deduced as

$$\sigma_{\gamma\gamma}^{\max} = \frac{\sum_{E_{\text{mean}}-100}^{E_{\text{mean}}+100} F(E)/\epsilon}{N_T W_{1\to gs}(\vartheta,\varphi)\int_{E_{\text{mean}}-100}^{E_{\text{mean}}+100} \Phi_\gamma(E)dE}, \qquad (11)$$

with $F(E)$ being the entire counts per channel at energy E. Thus, the according limit $\sigma_\gamma^{\max} = \sigma_{\gamma\gamma}^{\max} + \sigma_{\gamma\gamma'}$ for the total strength, shown in Fig. 10 as the height of the gray framed bars, includes all unresolved strength and it is independent of simulations.

Considering that $\sigma_\gamma^{\max}$ not only includes individual peaks and unresolved strength but also natural and atomic background, as well as detector response, the difference to the cross sections from Ref. [17] is still considerably high. Although inelastic decays, which decay not via the 2_1^+ level, are still not considered, the difference cannot be completely ascribed to this effect.

3. *Average branching ratio to the ground state*

Finally, the so-called mean branching ratio $\langle b_0\rangle$ of all states excited in the energy range covered by the photon flux to the ground state can be determined for the five beam settings. By considering only resolved strength, for the elastic scattering cross section its lower limit is defined via

$$\langle b_0\rangle^{\min} = \frac{\sigma_{\gamma\gamma}}{\sigma_\gamma} = \frac{\sigma_{\gamma\gamma}}{\sigma_{\gamma\gamma} + \sigma_{\gamma\gamma'}}. \qquad (12)$$

The terms $\sigma_{\gamma\gamma}$ and $\sigma_{\gamma\gamma'}$ denote the elastic and inelastic cross sections as defined in the previous section. Again assuming that inelastic decays occur predominantly via the 2_1^+ state an upper limit $\langle b_0\rangle^{\max}$, which considers unresolved strength in the elastic decay channel, can be determined by replacing $\sigma_{\gamma\gamma}$ via $\sigma_{\gamma\gamma}^{\max}$ in Eq. (12):

$$\langle b_0\rangle^{\max} = \frac{\sigma_{\gamma\gamma}^{\max}}{\sigma_{\gamma\gamma}^{\max} + \sigma_{\gamma\gamma'}} > \langle b_0\rangle^{\min}, \qquad (13)$$

with the true value for $\langle b_0\rangle$ lying between $\langle b_0\rangle^{\min}$ and $\langle b_0\rangle^{\max}$.

The average branching ratio $\langle b_0\rangle$ was also determined from calculations within the statistical model that were performed exploiting the DICEBOX code [41,56]. In DICEBOX so-called nuclear realizations of level sets and partial decay widths are created for a given nucleus. Up to a certain energy (up to which the nuclear levels and their spectroscopic properties are measured) experimental data is used to create the nuclear realization. Above this energy excited states are obtained by discretizing a level density formula. For each of these states partial radiation widths to all lower-lying states are randomly distributed in accordance with photon strength functions (PSFs) for $E1$, $M1$, and $E2$ strengths, taking into account Porter-Thomas fluctuations [57].

Finally, in analogy to an NRF experiment, γ cascades within a nuclear realization are initialized by exciting the levels of the simulated nucleus from its ground state considering a desired photon flux distribution. For each individual γ-cascade event the energies, spins, parities, and total radiation widths of each intermediate state, which is involved in the cascade, can be extracted from DICEBOX. For further information see Ref. [41].

The number of decays of dipole excited states decaying directly back to the ground state, as well as the number of decays of the 2_1^+ level to the ground state, can be obtained from the γ-cascade simulations. Using these numbers, the mean branching ratio $\langle b_0 \rangle$ can be determined from the simulations in exactly the same definition as in the experiment. Thus, experiment and simulation can directly be compared.

During the simulations, the back-shifted Fermi gas (BSFG) model served as input for the description of the level density in DICEBOX. The necessary parameters were taken from Ref. [58]. Lorentz functions were used to parametrize the PSFs [59]. The parameters of the Lorentz curve describing the $E1$ strength stem from a fit to (γ, n) reaction data [60]. Corresponding parameters for the $E2$ strength were extracted from elastic ^{3}He scattering reactions off ^{94}Mo [61]. Finally, the parameters for the $M1$ strength were deduced considering a global parametrization of $M1$ spin-flip resonances, which is proposed in Ref. [62]. However, the $M1$ and $E2$ PSFs do not influence the results significantly. The latter differ only slightly within the uncertainties, when both PSFs are set to zero.

Simulations were conducted with two different photon-flux distributions. On the one hand, the experiments at HIγS were simulated with help of the real photon-flux distributions (see Sec. II B). On the other hand, simulations in 200 keV wide energy bins with constant photon flux were done.

For each combination of photon-flux distribution and energy setting, 100 nuclear realizations each with 10^5 γ-cascade events were simulated. The $\langle b_0 \rangle$ value was calculated according to Eq. (12) for each nuclear realization and, finally, averaged over all 100 realizations.

The results for the mean branching ratio $\langle b_0 \rangle$ to the ground state are shown in Fig. 11(a). The experimentally deduced points are plotted with red circles and triangles, where the circles represent $\langle b_0 \rangle^{\mathrm{min}}$ and the triangles denote $\langle b_0 \rangle^{\mathrm{max}}$, respectively. The horizontal uncertainty bars mark the width of the photon flux distribution for each energy setting. The averaged values $\langle b_0 \rangle^{\mathrm{sim}}$ that were extracted from the simulations with real photon-flux distributions from HIγS are plotted with blue squares. The uncertainty bars correspond to the standard deviation of the average value within the 100 realizations. The standard deviations of the averaged $\langle b_0 \rangle$ values from the simulations with 200 keV wide bins are represented by the blue colored area. The standard deviations increase at lower energies due to the low level density and the corresponding large fluctuations in the statistical properties in this energy range.

The experimentally determined average branching ratio $\langle b_0 \rangle^{\mathrm{min}}$ to the ground state takes values between 45% and 65%. Thus, a considerable amount of strength branches to other states than the ground state. The mean branching ratio exhibits a maximum at about 6.4 MeV, indicating a larger ground-state branching ratio of the dipole excited states in the energy range between 5.5 and 7.5 MeV as in neighboring regions. This observation also holds for the upper limit $\langle b_0 \rangle^{\mathrm{max}}$. It takes values between 63% and 77% and exhibits a little less pronounced maximum at 6.4 MeV.

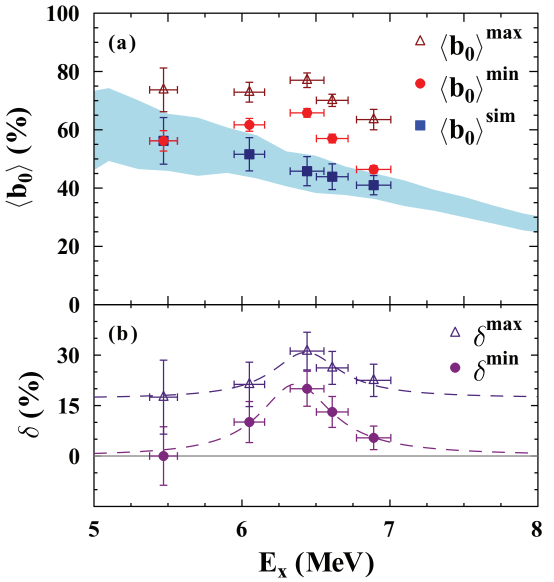

FIG. 11. (Color online) (a) Average branching ratios $\langle b_0 \rangle^{\mathrm{min}}$ (red circles) and $\langle b_0 \rangle^{\mathrm{max}}$ (red triangles) determined from the experiment at HIγS, as well as from simulations within the statistical model (blue squares and shaded area). (b) Differences between the experimentally deduced mean branching ratios $\langle b_0 \rangle^{\mathrm{min}}$ (purple circles), as well as $\langle b_0 \rangle^{\mathrm{max}}$ (purple triangles) and the corresponding simulated values $\langle b_0 \rangle^{\mathrm{sim}}$. The dashed lines are fits of Lorentz functions to the data points.

The $\langle b_0 \rangle^{\mathrm{sim}}$ values extracted from the DICEBOX simulations describe the experimental data points $\langle b_0 \rangle^{\mathrm{min}}$ at 5.47 and 6.89 MeV well. However, the three points in between at 6.05, 6.44, and 6.61 MeV cannot be reproduced by DICEBOX using a simple Lorentz parametrization for the $E1$ PSF. Since the upper limit for the average branching ratio is even higher it cannot be reproduced at all. In particular the simulations with 200 keV wide bins of constant photon flux clarify that the $\langle b_0 \rangle^{\mathrm{sim}}$ values exhibit no maximum like the experimental data if a Lorentz parametrization is used to describe the $E1$ PSF. The simulated values decrease smoothly over the entire energy range.

The differences $\delta^{\mathrm{min}} = \langle b_0 \rangle^{\mathrm{min}} - \langle b_0 \rangle^{\mathrm{sim}}$ (purple circles) and $\delta^{\mathrm{max}} = \langle b_0 \rangle^{\mathrm{max}} - \langle b_0 \rangle^{\mathrm{sim}}$ (purple triangles) between the experimentally and the corresponding simulated values for the average branching ratio to the ground state are shown in Fig. 11(b). They represent the amount of relative decay strength into the ground state, which cannot be reproduced by statistical models, i.e., the strength corresponding to a distinct, nonstatistical structure. The curves show fits of Lorentz functions to the data points. The maximum of the Lorentz function fitted to δ^{min} is located at 6.36 MeV and the width is given by 0.59 MeV. In the case of δ^{max} the Lorentz function is displaced by a constant offset of 17%. Its maximum is shifted to 6.43 MeV and with a width of 0.56 MeV it is a little narrower than the fit to δ^{min}. However, it still exhibits a distinct maximum. Thus, we conclude the existence of a nonstatistical structure of $E1$ excitation near 6.4 MeV excitation energy. Alternatively, this structure may be ascribed to the so-called "elastic enhancement" that was discussed, e.g., in Ref. [63]. It states that strongly excited states decay preferentially directly back to the ground state. In this scenario, the fact of an apparent concentration of large Γ_0 values concentrated in a few 1^- states near 6.4 MeV excitation energy again hints at a localized structural feature.

A similar behavior of the average ground-state branching ratio was reported in the isotope ^{60}Ni [14,15]. In the energy range of strongly excited electric dipole levels, the mean branching ratio to the ground state is about 70% to 80%. At higher energies, where the excitation strength of the individual 1^- states decreases, this ratio drops to about 50% to 60%. Furthermore, the number of low-lying levels that are populated via inelastic decays increases towards higher energies of the incident photon beam indicating a more complex structure of the excited states.

In Ref. [14], these observations for ^{60}Ni are associated with the microscopic description of electric dipole states in the framework of the QPM. The latter shows that 1^- states resulting from 1p1h excitations have low branches to intermediate states. The inelastic decay occurs predominantly to one-phonon (e.g., the 2_1^+) or two-phonon (e.g., 2_2^+ and 0_2^+) levels. At higher energies, the wave functions exhibit more complex components opening more decay channels and, thus, resulting in larger inelastic branches, i.e., smaller $\langle b_0 \rangle$.

V. SUMMARY

Photon scattering experiments on the open-shell nucleus ^{94}Mo have been performed to study its photoresponse up to 8.7 MeV. At the DHIPS facility at the S-DALINAC two measurements with unpolarized bremsstrahlung photons with endpoint energies of 7.65 and 8.7 MeV were performed. In addition, the nearly monochromatic, linearly polarized photon beam of HIγS was used to investigate ^{94}Mo at 5.47, 6.05, 6.44, 6.61, and 6.89 MeV mean beam energies.

Although the level density of ^{94}Mo is already rather high in comparison to nuclei with at least one closed major shell, we managed to resolve even close lying peaks in the spectra corresponding to individual states. In total, 83 excited states of ^{94}Mo were observed up to 8 MeV excitation energy. The spin quantum number and the transition strength were unknown for 78 excited states. To each of these 78 states spin $J = 1$ was assigned. The parity quantum number was determined for 41 of the dipole excited states. One state has positive parity quantum number, the others have negative parity.

For all observed states the product Γ_0^2/Γ of the ground-state transition width Γ_0 and the branching ratio Γ_0/Γ to the ground state was determined. The $B(E1)\uparrow$ and $B(M1)\uparrow$ strengths, respectively, were calculated for all observed transitions.

The resulting $B(E1)\uparrow$-strength distribution was compared to a microscopic calculation within the QPM. The QPM calculation describes the experimentally deduced distribution, as well as the fragmentation of the strength well.

The measurements at HIγS revealed a different decay pattern of the dipole excited states in the energy region from 5.5 to 7.5 MeV and below it.

The asymmetry of the distribution of the decay photons of the 2_1^+ level indicates a varying decay pattern of the states in the region between 5.5 and 7.5 MeV. While, on average, the states at about 5.5 MeV decay to 55% directly to the ground state, and those which decay via intermediate states decay dominantly via γ cascades, the picture for the excited states from 5.5 to 7.5 MeV is different. They have an enhanced branching ratio to the ground state and inelastic decays occur predominantly directly to the 2_1^+ level.

The branching ratio was also deduced from simulations within the statistical model, which were performed exploiting the DICEBOX code. However, the experimentally observed enhancement cannot be reproduced in the statistical model using simple Lorentz parametrizations. This indicates a structural change in the energy range between 5.5 and 7.5 MeV where we locate a structure with enhanced decay to the ground state. This is an interesting observation with respect to the current discussion of the pygmy dipole resonance. In Refs. [14,15] similar observations in ^{60}Ni were connected to 1p1h excitations in the energy range of enhanced branching to the ground state, while at higher energies more complex components mix into the wave function.

However, the total cross section, which also takes decays via intermediate states into account, does not show a maximum in the investigated energy range for ^{94}Mo. The inelastic cross section smoothly increases towards higher energies and compensates for the decreasing elastic cross section. The total cross section was compared to corresponding values from another NRF experiment, reported previously in Ref. [17], that were determined with a different analyzing technique. The considerable discrepancy even to the upper limit for the total cross section that was extracted from our measurements may be explained with dipole excited states decaying via intermediate states without populating the 2_1^+ level. However, this effect is expected to be much smaller.

ACKNOWLEDGMENTS

The authors thank Ralf Eichhorn and the S-DALINAC group for providing the electron beam. We also thank the operators team of Duke Free Electron Laser Laboratory for their kind hospitality and the support during the preparation of the setup and during the measurements. Furthermore, we acknowledge the help of all scientists on shift during the measurements. We thank M. Fritzsche and G. Rusev for support during the measurements and for discussions, as well as M. Krtička for providing the DICEBOX code and for discussions during the simulations. We further thank R. Schwengner for helpful discussions. J.G. and A.S. acknowledge support by HIC for FAIR. This work was supported by the Deutsche Forschungsgemeinschaft (Contract No. SFB 634, SO907/2-1, and ZI510/4-2), by the Alliance Program of the Helmholtz Association (HA216/EMMI), as well as by US DOE Grants No. DE-FG02-97ER41033 and No. DE-FG02-97ER41042.

[1] M. N. Harakeh and A. van der Woude, *Giant Resonances* (Oxford University Press, Oxford, 2001).

[2] W. Greiner and J. A. Maruhn, *Nuclear Models* (Springer, Berlin, 1996).

[3] G. A. Bartholomew, Annu. Rev. Nucl. Sci. **11**, 259 (1961).

[4] J. S. Brzosko, E. Gierlik, A. Soltan, Jr., and Z. Wilhelmi, Can. J. Phys. **47**, 2849 (1969).

[5] G. A. Bartholomew, E. D. Earle, A. J. Ferguson, J. W. Knowles, and M. A. Lone, Adv. Nucl. Phys. **7**, 229 (1973).

[6] D. Savran, T. Aumann, and A. Zilges, Prog. Part. Nucl. Phys. **70**, 210 (2013).

[7] R. Mohan, M. Danos, and L. C. Biedenharn, Phys. Rev. C **3**, 1740 (1971).

[8] N. Paar, D. Vretenar, E. Khan, and G. Colò, Rep. Prog. Phys. **70**, 691 (2007).

[9] U. Kneissl, H. Pitz, and A. Zilges, Prog. Part. Nucl. Phys. **37**, 349 (1996).

[10] U. Kneissl, N. Pietralla, and A. Zilges, J. Phys. G: Nucl. Part. Phys. **32**, R217 (2006).

[11] T. Hartmann, M. Babilon, S. Kamerdzhiev, E. Litvinova, D. Savran, S. Volz, and A. Zilges, Phys. Rev. Lett. **93**, 192501 (2004).

[12] J. Isaak, D. Savran, M. Fritzsche, D. Galaviz, T. Hartmann, S. Kamerdzhiev, J. H. Kelley, E. Kwan, N. Pietralla, C. Romig, G. Rusev, K. Sonnabend, A. P. Tonchev, W. Tornow, and A. Zilges, Phys. Rev. C **83**, 034304 (2011).

[13] F. Bauwens, J. Bryssinck, D. De Frenne, K. Govaert, L. Govor, M. Hagemann, J. Heyse, E. Jacobs, W. Mondelaers, and V. Yu. Ponomarev, Phys. Rev. C **62**, 024302 (2000).

[14] M. Scheck, V. Yu. Ponomarev, T. Aumann, J. Beller, M. Fritzsche, J. Isaak, J. H. Kelley, E. Kwan, N. Pietralla, R. Raut, C. Romig, G. Rusev, D. Savran, K. Sonnabend, A. P. Tonchev *et al.*, Phys. Rev. C **87**, 051304 (2013).

[15] M. Scheck, V. Yu. Ponomarev, M. Fritzsche, J. Joubert, T. Aumann, J. Beller, J. Isaak, J. H. Kelley, E. Kwan, N. Pietralla, R. Raut, C. Romig, G. Rusev, D. Savran, L. Schnorrenberger *et al.*, Phys. Rev. C **88**, 044304 (2013).

[16] A. Jung, S. Lindenstruth, H. Schacht, B. Starck, R. Stock, C. Wesselborg, R. Heil, U. Kneissl, J. Margraf, H. Pitz, and F. Steiper, Nucl. Phys. A **584**, 103 (1995).

[17] G. Rusev, R. Schwengner, R. Beyer, M. Erhard, E. Grosse, A. R. Junghans, K. Kosev, C. Nair, K. D. Schilling, A. Wagner, F. Dönau, and S. Frauendorf, Phys. Rev. C **79**, 061302(R) (2009).

[18] M. Erhard, A. R. Junghans, C. Nair, R. Schwengner, R. Beyer, J. Klug, K. Kosev, A. Wagner, and E. Grosse, Phys. Rev. C **81**, 034319 (2010).

[19] K. Govaert, F. Bauwens, J. Bryssinck, D. De Frenne, E. Jacobs, W. Mondelaers, L. Govor, and V. Yu. Ponomarev, Phys. Rev. C **57**, 2229 (1998).

[20] B. Özel, J. Enders, P. von Neuman Cosel, I. Poltoratska, A. Richter, D. Savran, S. Volz, and A. Zilges, Nucl. Phys. A **788**, 385 (2007).

[21] N. Ryezayeva, T. Hartmann, Y. Kalmykov, H. Lenske, P. von Neumann-Cosel, V. Yu. Ponomarev, A. Richter, A. Shevchenko, S. Volz, and J. Wambach, Phys. Rev. Lett. **89**, 272502 (2002).

[22] J. Enders, P. von Brentano, J. Eberth, A. Fitzler, C. Fransen, R.-D. Herzberg, H. Kaiser, L. Käubler, P. von Neumann-Cosel, N. Pietralla, V. Yu. Ponomarev, A. Richter, R. Schwengner, and I. Wiedenhöver, Nucl. Phys. A **724**, 243 (2003).

[23] R. Schwengner, R. Massarczyk, G. Rusev, N. Tsoneva, D. Bemmerer, R. Beyer, R. Hannaske, A. R. Junghans, J. H. Kelley, E. Kwan, H. Lenske, M. Marta, R. Raut, K. D. Schilling, A. Tonchev *et al.*, Phys. Rev. C **87**, 024306 (2013).

[24] R. Schwengner, G. Rusev, N. Benouaret, R. Beyer, M. Erhard, E. Grosse, A. R. Junghans, J. Klug, K. Kosev, L. Kostov, C. Nair, N. Nankov, K. D. Schilling, and A. Wagner, Phys. Rev. C **76**, 034321 (2007).

[25] N. Benouaret, R. Schwengner, G. Rusev, F. Dönau, R. Beyer, M. Erhard, E. Grosse, A. R. Junghans, K. Kosev, C. Nair, K. D. Schilling, A. Wagner, and N. Bendjaballah, Phys. Rev. C **79**, 014303 (2009).

[26] R. Schwengner, G. Rusev, N. Tsoneva, N. Benouaret, R. Beyer, M. Erhard, E. Grosse, A. R. Junghans, J. Klug, K. Kosev, H. Lenske, C. Nair, K. D. Schilling, and A. Wagner, Phys. Rev. C **78**, 064314 (2008).

[27] A. Zilges, S. Volz, M. Babilon, T. Hartmann, P. Mohr, and K. Vogt, Phys. Lett. B **542**, 43 (2002).

[28] S. Volz, N. Tsoneva, M. Babilon, M. Elvers, J. Hasper, R.-D. Herzberg, H. Lenske, K. Lindenberg, D. Savran, and A. Zilges, Nucl. Phys. A **779**, 1 (2006).

[29] D. Savran, M. Fritzsche, J. Hasper, K. Lindenberg, S. Müller, V. Yu. Ponomarev, K. Sonnabend, and A. Zilges, Phys. Rev. Lett. **100**, 232501 (2008).

[30] D. Savran, M. Elvers, J. Endres, M. Fritzsche, B. Löher, N. Pietralla, V. Yu. Ponomarev, C. Romig, L. Schnorrenberger, K. Sonnabend, and A. Zilges, Phys. Rev. C **84**, 024326 (2011).

[31] P. Adrich, A. Klimkiewicz, M. Fallot, K. Boretzky, T. Aumann, D. Cortina-Gil, U. D. Pramanik, T. W. Elze, H. Emling, H. Geissel, M. Hellström, K. L. Jones, J. V. Kratz, R. Kulessa, Y. Leifels *et al.* (LAND-FRS Collaboration), Phys. Rev. Lett. **95**, 132501 (2005).

[32] A. Klimkiewicz, N. Paar, P. Adrich, M. Fallot, K. Boretzky, T. Aumann, D. Cortina-Gil, U. D. Pramanik, T. W. Elze, H. Emling, H. Geissel, M. Hellström, K. L. Jones, J. V. Kratz, R. Kulessa *et al.* (LAND Collaboration), Phys. Rev. C **76**, 051603 (2007).

[33] O. Wieland, A. Bracco, F. Camera, G. Benzoni, N. Blasi, S. Brambilla, F. C. L. Crespi, S. Leoni, B. Million, R. Nicolini, A. Maj, P. Bednarczyk, J. Grebosz, M. Kmiecik, W. Meczynski *et al.*, Phys. Rev. Lett. **102**, 092502 (2009).

[34] D. Savran, M. Babilon, A. M. van den Berg, M. N. Harakeh, J. Hasper, A. Matic, H. J. Wörtche, and A. Zilges, Phys. Rev. Lett. **97**, 172502 (2006).

[35] J. Endres, D. Savran, A. M. van den Berg, P. Dendooven, M. Fritzsche, M. N. Harakeh, J. Hasper, H. J. Wortche, and A. Zilges, Phys. Rev. C **80**, 034302 (2009).

[36] J. Endres, E. Litvinova, D. Savran, P. A. Butler, M. N. Harakeh, S. Harissopulos, R.-D. Herzberg, R. Krücken, A. Lagoyannis, N. Pietralla, V. Yu. Ponomarev, L. Popescu, P. Ring, M. Scheck, K. Sonnabend *et al.*, Phys. Rev. Lett. **105**, 212503 (2010).

[37] R. Massarczyk, R. Schwengner, F. Dönau, E. Litvinova, G. Rusev, R. Beyer, R. Hannaske, A. R. Junghans, M. Kempe, J. H. Kelley, T. Kögler, K. Kosev, E. Kwan, M. Marta, A. Matic *et al.*, Phys. Rev. C **86**, 014319 (2012).

[38] N. Pietralla, C. Fransen, D. Belic, P. von Brentano, C. Frießner, U. Kneissl, A. Linnemann, A. Nord, H. H. Pitz, T. Otsuka, I. Schneider, V. Werner, and I. Wiedenhöver, Phys. Rev. Lett. **83**, 1303 (1999).

[39] C. Fransen, N. Pietralla, Z. Ammar, D. Bandyopadhyay, N. Boukharouba, P. von Brentano, A. Dewald, J. Gableske, A. Gade, J. Jolie, U. Kneissl, S. R. Lesher, A. F. Lisetskiy, M. T. McEllistrem, M. Merrick *et al.*, Phys. Rev. C **67**, 024307 (2003).

[40] V. G. Soloviev, *Theory of Atomic Nuclei, Quasi-particle and Phonons* (Taylor & Francis, London, 1992).

[41] F. Bečvář, Nucl. Instrum. Methods A **417**, 434 (1998).

[42] K. Sonnabend, D. Savran, J. Beller, M. Büssing, A. Constantinescu, M. Elvers, J. Endres, M. Fritzsche, J. Glorius, J. Hasper, J. Isaak, B. Löher, S. Müller, N. Pietralla, C. Romig *et al.*, Nucl. Instrum. Methods A **640**, 6 (2011).

[43] H. R. Weller, M. W. Ahmed, H. Gao, W. Tornow, Y. K. Wu, M. Gai, and R. Miskimen, Prog. Part. Nucl. Phys. **62**, 257 (2009).

[44] V. Litvinenko, B. Burnham, S. Park, Y. Wu, R. Cataldo, M. Emamian, J. Faircloth, S. Goetz, N. Hower, J. Madey, J. Meyer, P. Morcombe, O. Oakeley, J. Patterson, G. Swift *et al.*, Nucl. Instrum. Methods Phys. Res., Sect. A **407**, 8 (1998).

[45] S. Agostinelli, J. Allison, K. Amako, J. Apostolakis, H. Araujo, P. Arce, M. Asai, D. Axen, S. Banerjee, G. Barrand, F. Behner, L. Bellagamba, J. Boudreau, L. Broglia, A. Brunengo *et al.*, Nucl. Instrum. Methods A **506**, 250 (2003).

[46] M. A. Büssing, M. Elvers, J. Endres, J. Hasper, A. Zilges, M. Fritzsche, K. Lindenberg, S. Müller, D. Savran, and K. Sonnabend, Phys. Rev. C **78**, 044309 (2008).

[47] C. Hutter, M. Babilon, W. Bayer, D. Galaviz, T. Hartmann, P. Mohr, S. Müller, W. Rochow, D. Savran, K. Sonnabend, K. Vogt, S. Volz, and A. Zilges, Nucl. Instrum. Methods A **489**, 247 (2002).

[48] B. Alikhani, A. Givechev, A. Heinz, P. John, J. Leske, M. Lettmann, O. Möller, N. Pietralla, and C. Röder, Nucl. Instrum. Methods A **675**, 144 (2012).

[49] N. Pietralla, Z. Berant, V. N. Litvinenko, S. Hartman, F. F. Mikhailov, I. V. Pinayev, G. Swift, M. W. Ahmed, J. H. Kelley, S. O. Nelson, R. Prior, K. Sabourov, A. P. Tonchev, and H. R. Weller, Phys. Rev. Lett. **88**, 012502 (2001).

[50] D. Abriola and A. Sonzogni, Nucl. Data Sheets **107**, 2423 (2006).

[51] V. Derya, J. Endres, M. Elvers, M. Harakeh, N. Pietralla, C. Romig, D. Savran, M. Scheck, F. Siebenhühner, V. Stoica, H. Wörtche, and A. Zilges, Nucl. Phys. A **906**, 94 (2013).

[52] G. Rusev, N. Tsoneva, F. Dönau, S. Frauendorf, R. Schwengner, A. P. Tonchev, A. S. Adekola, S. L. Hammond, J. H. Kelley, E. Kwan, H. Lenske, W. Tornow, and A. Wagner, Phys. Rev. Lett. **110**, 022503 (2013).

[53] N. Lo Iudice and F. Palumbo, Phys. Rev. Lett. **41**, 1532 (1978).

[54] D. Bohle, A. Richter, W. Steffen, A. Dieperink, N. L. Iudice, F. Palumbo, and O. Scholten, Phys. Lett. B **137**, 27 (1984).

[55] A. P. Tonchev, S. L. Hammond, J. H. Kelley, E. Kwan, H. Lenske, G. Rusev, W. Tornow, and N. Tsoneva, Phys. Rev. Lett. **104**, 072501 (2010).

[56] C. T. Angell, S. L. Hammond, H. J. Karwowski, J .H. Kelley, M. Krticka, E. Kwan, A. Makinaga, and G. Rusev, Phys. Rev. C **86**, 051302 (2012).

[57] C. E. Porter and R. G. Thomas, Phys. Rev. **104**, 483 (1956).

[58] T. von Egidy and D. Bucurescu, Phys. Rev. C **72**, 044311 (2005).

[59] P. Axel, Phys. Rev. **126**, 671 (1962).

[60] H. Beil, R. Bergère, P. Carlos, A. Leprêtre, A. D. Miniac, and A. Veyssière, Nucl. Phys. A **227**, 427 (1974).

[61] A. Moalem, Y. Gaillard, A. M. Bemolle, M. Buenerd, J. Chauvin, G. Duhamel, D. Lebrun, P. Martin, G. Perrin, and P. de Saintignon, Phys. Rev. C **20**, 1593 (1979).

[62] T. Belgya, O. Bersillon, R. Capote, T. Fukahori, G. Zhigang, S. Goriely, M. Herman, A. Ignatyuk, S. Kailas, A. Koning, P. Oblozinsky, V. Plujko, and P. Young, *Handbook for Calculations of Nuclear Reaction Data, RIPL-2*, IAEA-TECDOC-1506 (IAEA, Vienna, 2006) http://www-nds.iaea.org/RIPL-2/

[63] P. Axel, K. K. Min, and D. C. Sutton, Phys. Rev. C **2**, 689 (1970).